



Supporting Online Material for
**The Molecular Architecture of Axonemes Revealed by Cryoelectron
Tomography**

Daniela Nicastro,* Cindi Schwartz, Jason Pierson, Richard Gaudette, Mary E. Porter,
J. Richard McIntosh

*To whom correspondence should be addressed. E-mail: nicastro@colorado.edu

Published 18 August 2006, *Science* **313**, 944 (2006)

DOI: 10.1126/science.1128618

This PDF file includes:

Materials and Methods
SOM Text
Figs. S1 to S4
References

Other Supporting Online Material for this manuscript includes the following:
(available at www.sciencemag.org/cgi/content/full/313/5789/944/DC1)

Movies S1 to S6

SUPPORTING ONLINE MATERIAL

Materials and Methods

SOM Text: 3D correlation averaging for electron tomography

Figs. S1 to S4

References

Movie Legends S1 to S6

Materials and Methods:

Specimen Preparation

Live sea urchins (*Spaerechinus purpuratus* from Santa Barbara Marine Biologicals, C. Hollahan, admin@sbmarinebio.com) were kept at 12°C for up to 8 month in artificial seawater. Spawning was induced, and the collected sperm were kept on ice without dilution as described (S1).

The wild type (137c) and *pf9-3* (S2) mutant strains of *Chlamydomonas reinhardtii* were maintained on solid medium and resuspended into liquid medium to induce regeneration of flagella. Flagella were isolated by pH shock and demembrated with 0.1% Nonidet-P-40 in HMEEN buffer (HMEEN buffer, which is 25 mM NaCl, 10 mM Hepes, pH 7.4, 2.5 mM MgSO₄, 1 mM EGTA, 0.1 mM EDTA). Axonemes were collected by centrifugation, resuspended in HMEEN buffer, and shipped on wet ice by overnight express as described in (S2, S3).

Carbon-coated Quantifoil grids (Quantifoil Micro Tools, GmbH, Jena, Germany) were glow discharged before use. 5 µl of a 10 nm colloidal gold solution (Sigma, St. Louis, MO) was applied and dried, then the grid was quickly rinsed in distilled water and dried before applying 5 µl of sperm or isolated *Chlamydomonas* axonemes. Excessive fluid was blotted from the grid with filter paper before plunge freezing the grid in liquid ethane (S4). The vitrified sample was then stored in a liquid nitrogen Dewar.

Electron microscopy

The grids were mounted in a $\pm 70^\circ$ cryo-tilt holder (Gatan, Pleasanton, CA) and cryo-transferred into a Tecnai F-30 microscope (FEI, Eindhoven Netherlands) equipped with a post-column energy filter (GIF 2002, Gatan, Pleasanton, CA). More than 40 single-axis tilt series were recorded digitally under low-dose conditions using the automated tilt-series acquisition software, SerialEM (S5). The specimen was tilted over a total angular range of about -65° to $+65^\circ$ with 1° - 1.5° increments and a cumulative electron dose to the specimen below 100 electrons/Å². The energy filter was operated in the zero-energy-loss mode with a slit width of 20 eV. At the chosen magnification the pixel size in unbinned images was 0.95 nm. Images were recorded 6-8 µm under focus to enhance contrast (first CTF zero at $1/3.5 \text{ nm}^{-1}$ and $1/4 \text{ nm}^{-1}$).

For the freeze-etching experiments the cryo-holder was transferred to the TEM and then heated with the GATAN heat controller to -125°C for 1 hour with the TEM-cryo-box

inserted. After enough ice had sublimated the specimen was again cooled to $\sim -190^{\circ}\text{C}$, and tilt series were recorded as described above.

Image processing

The tilt series images were aligned using fiducial markers, reconstructed by weighted back-projection, analyzed and graphically modeled using the IMOD software package (S6). Unless otherwise stated, all surface- and volume-rendering visualizations were done without manual contouring or feature enhancement using the AMIRA 3D visualization package (TGS, Mercury Computer Systems, San Diego, CA). For 3D correlation averaging we programmed our own software and the major processing steps are described in the SOM Text below. By taking advantage of the cylindrical arrangement of the doublets, we compensated for the data that are typically missing in an EM tilt series that provides the data for tomographic reconstruction. The resulting averages were essentially isotropic in resolution and contrast. Images of raw tomograms are shown in Figs. 1A,B, S1E,F, S4D-E; all other tomographic slices are from volume averages with the following number of particles included in the average: Figs. 4J,K (n=120); Figs. 3A, 4A-D, S2B-F, S3A-F (n=150); Figs. 1F,H, 2E, 3B,E,F,H, S2A,G-K (n=160); Figs. 1C,E, 2A-C, 4G-I (n=280); Fig. 1D-inset (n=560). (See Fig. S1 for methodical details.)

SOM Text: 3D correlation averaging for electron tomography.

Electron tomography (ET) is a powerful tool that allows the study of macromolecular structures in situ; extending the technique to cryo-ET allows to observe cells and macromolecular complexes in a near-native state. Due to beam induced specimen damage, however, the electron dose that a sample can sustain is limited. This in turn limits the signal-to-noise ratio (SNR) of the projection images and reconstructed volumes. If the structure under study is present in multiple copies in one or many tomograms, one can improve the image SNR by statistical estimation, based on all the instances available. To exploit this opportunity we developed a set of processing tools to excise particles of interest from one or several tomograms, align them with one another, and estimate the average 3D distribution of electron density, based on the aligned particles. Our algorithm builds on the single-particle electron microscopy approach, but alignment and voxel estimation are carried out over the 3D tomographic volume (S7, S8). The advantage of this approach over single particle averaging is that the structure of interest can be studied in situ instead of having to be isolated from its cellular context. Below are the major processing steps of the algorithm.

Alignment Transformation Initialization

Since the alignment transform search is by far the most computationally costly step of the process, any a priori information that can limit the scope of this search is useful. For the estimation of the axonemal subunits presented here, we used the well-defined arrangement of the nine MT doublets as a constraint. Doublets are approximately evenly spaced around a circle in the cross-section of the axoneme, and subunits of the doublets are similarly oriented along the length of each fiber. This provided the information necessary to calculate

an approximate orientation of each particle as a place from which our search for optimal alignment could begin. This strategy resulted in a significant reduction in computational cost compared to a full Euler angle search.

Initial Reference Generation

The alignment transformation search step requires an initial reference to orient and anchor the search. We selected a single representative particle from the set of particles identified in the first step. To avoid a bias in the resulting estimation we used multiple search iterations and tested multiple randomly chosen references.

Alignment Transform Search

The orientation and position of a solid body in 3D space is uniquely described by three positional parameters, typically the Cartesian coordinates (x,y,z), and three rotational parameters, such as the Euler angles (ϕ , θ , φ). Our algorithm searches this six dimensional parameter space for the “best” alignment of each particle with the reference by sequentially applying a set of Euler rotations to the reference and recording the peak similarity measure over the range of translational shifts for each rotation. After explicitly applying each Euler rotation from the set, the maximum of the peak similarity measures identifies the “best” transformation for aligning the particle with the reference. The procedure is then repeated with the next particle. The alignment transform search for all particles and the reference generation are typically iterated. The search begins with a rather wide range of parameter values, which is sampled coarsely with the initial reference; it then goes to a narrow range centered around the initial best fit, now using finer sampling and a refined reference (see below) to obtain a good estimation of the optimal orientation for alignment. To calculate the local correlation coefficient sequence efficiently we developed a Fourier domain algorithm derived from the Fourier Correlation Theorem to calculate the varying terms as the region of interest shifts location.

Refined Reference Generation and Final Particle Estimation

Estimation of a refined reference and final density function is computed using a weighted average of the aligned particles. Because of the physical limitations in the data acquisition process, tomographic reconstructions are missing frequency information along lines at the angles of the missing projections (limited tilt angle range). This missing frequency information is commonly called the tomographic missing wedge. We implemented a weighted averaging algorithm that compensates for the tomographic missing wedge. Alignment of particles with different orientations relative to the tilt axis will cause the tomographic missing wedge for each particle to be oriented in different directions. By locating the missing wedge and mapping each valid (non-zero) Fourier component into the aligned volume, we filled in the missing wedge and correctly weight the average for each Fourier component that was present.

Algorithm Performance

To analyze the quantitative performance of our particle estimation algorithm and to estimate the spatial resolution achieved, we computed the Fourier Shell Correlation (FSC) and Spectral SNR (SSNR) of the reconstruction. Typical FSC and SSNR plots are shown in Figure S1G and S1H.

Figures S1 to S4 and Legends:

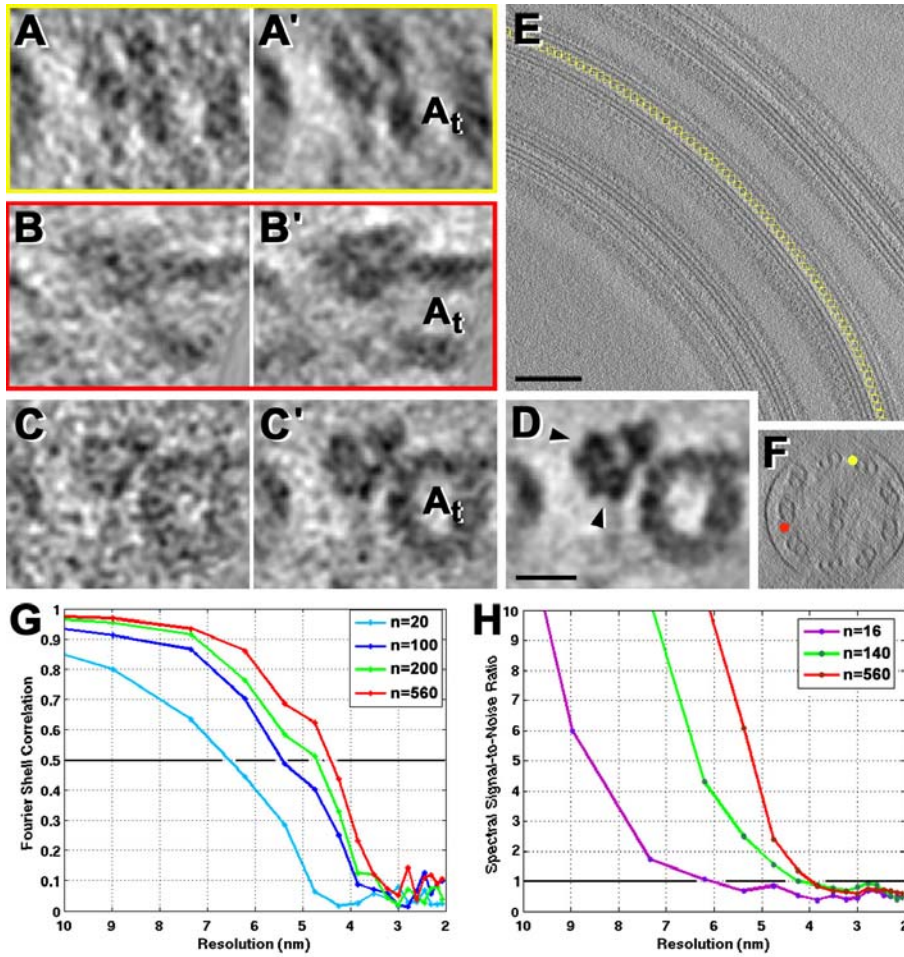


Fig. S1) 3D particle averaging and the resulting resolution improvement, demonstrated on ODAs of a frozen-hydrated and 3D reconstructed sea urchin sperm flagellum. (A-D) Slices through a 3D average of an A_r -tubule and the attached ODA complex in cross-sectional view of the MT from distal to proximal. The improvement in signal-to-noise ratio with increasing numbers of particles averaged can be seen by following the image pairs (A-A', B-B', C-C', and D): (A-C) 16 particles, (A'-C') 80 particles, and (D) 560 particles averaged. In (A-A' and B-B') ODA were averaged along one MT doublet only; yellow and pink color codes indicate positions of the ODAs in (E,F). Owing to the limited tilt-range, all raw tomograms contain artifacts that result from the 'missing-wedge', i.e., information missing perpendicular to the tilt-axis; note that the MT wall is not closed at the top and bottom in (A-A') or on the left and right side in (B-B'). By taking advantage of the cylindrical arrangement of the nine doublets we averaged objects viewed from multiple orientations and achieved essentially isotropic resolution and contrast (C-C' and D), thanks to the resulting compensation for the data missing from each individual particle. Particles from eight MT doublets with different orientations relative to

the tilt-axis were used to fill in the missing wedge; note that the result is a round MT cross-section. In (D) the averaging allowed us to visualize the dynein motor domains (*black arrowheads*). (E,F) ~20 nm thick longitudinal (E) and ~50 nm thick cross-sectional (F, viewed distal to proximal) tomographic slices from one of the reconstructed sea urchin sperm flagellum used for the averages in (A-D); MT doublet #1 (*red*) and #7 (*yellow*). (G,H) Example of Fourier Shell Correlation (G) and Spectral-Signal-to-Noise Ratio (H) curves of the particle averages of the ODAs; the different curves show the performance for a specific number of particles included in the average (see box in the image). As expected, when an increasing number of particles was included the SNR at a given resolution was improved. Note that for the average shown in (D) the resolution was estimated to be 4.3 nm (FSC=0.5 in G) or 4.0 nm (SNR=1 in H). Scale bars: (E) 200nm, (D) 15nm.

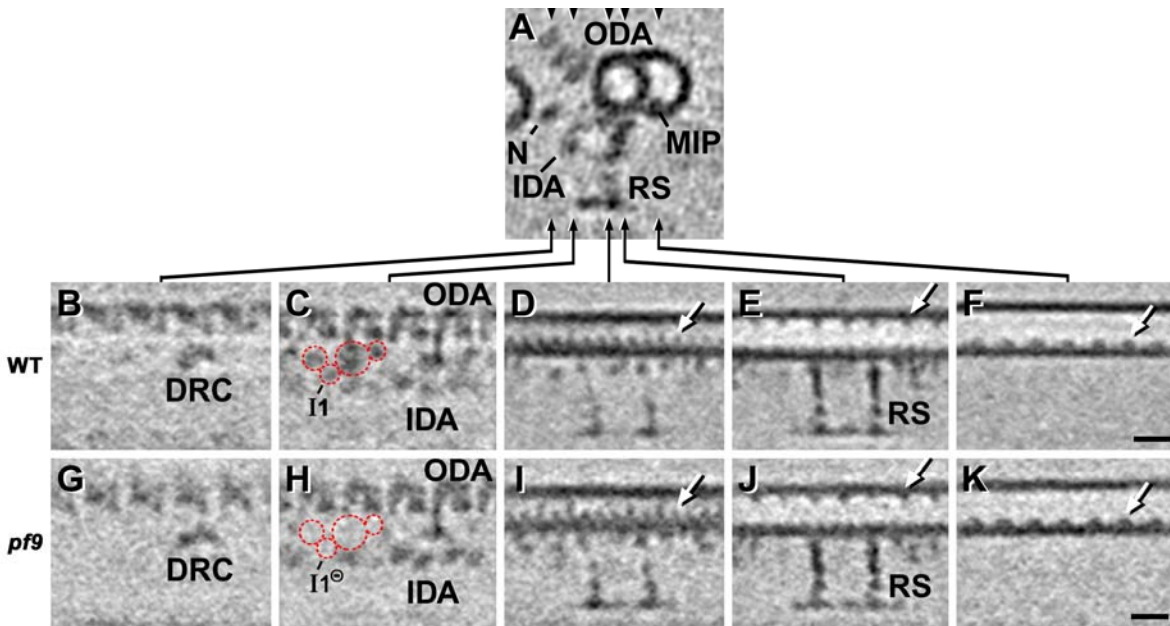


Fig. S2) Comparison of wild type (B-F) and *pf9*-mutant (A,G-K) axonemes from *Chlamydomonas*. (A-K) Tomographic slices through averages of 150 (B-F) and 160 (A,G-K) repeats, respectively; in the cross-sectional view (A) one can clearly identify the MT doublet, MT inner protein (*MIP*; see text Fig. 4 and below), the three dynein motor domains of the *ODA*, one head of the *IDA*, part of the nexin link (*N*) and a radial spoke (*RS*). *Black arrows* indicate the position of selected slices (B-F) and (G-K), respectively, that are in longitudinal orientation, viewed from the B-tubule of the adjacent doublet with proximal on the left. The slices of corresponding regions from wild type and the *pf9*-mutant showed their structural consistency with the exception of the missing *II* complex (*II*⁻) in the mutant. Note the distinct axial relationship of the MIPs to the protein complexes on the outside of the MTs (e.g., compare position of MIP2 to the radial spokes in E and J). *White arrows*, MIPs; *IDA/ODA*, inner and outer dynein arms; *DRC*, dynein regulatory complex. In (E and J) note the different structural domains along the radial spoke shafts (*RS*). Scale: 20nm.

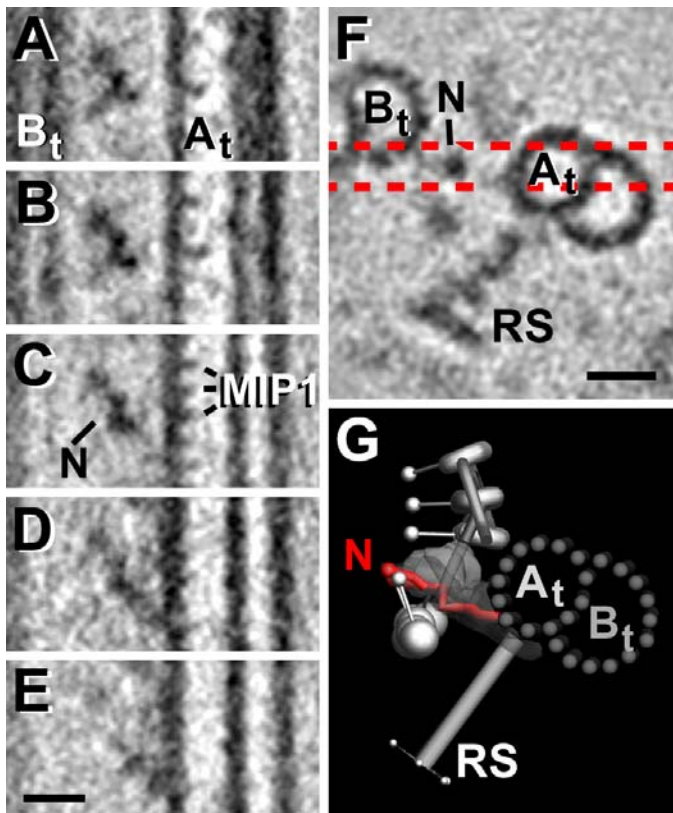


Fig. S3) The nexin link of wild type *Chlamydomonas*. (A-E) A series of tomographic slices through the nexin link (N) from peripheral towards the axoneme center; proximal is at the top; A_t/B_t, A- and B-tubule. MT inner proteins (MIP) are visible in several of these slices (e.g., S3C). (F) The orientation and range of the slices shown in (A-E) are indicated in the cross-sectional view (F) by dashed red lines; viewed from distal; RS, radial spoke. (G) Graphic model of the nexin link (N). The viewing orientation corresponds to (F). Scale: 20nm (E,F).

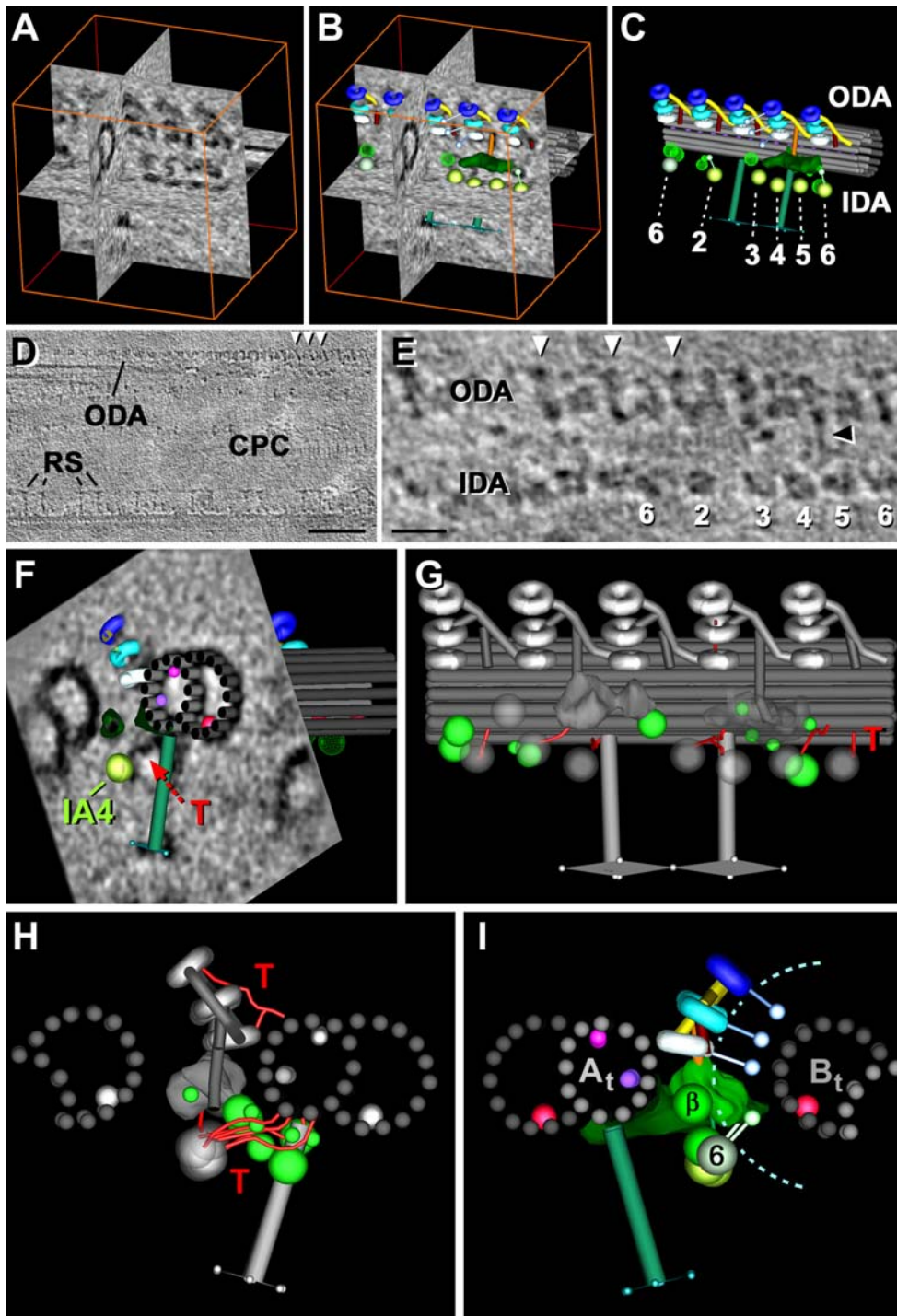


Fig. S4) Graphic modeling in IMOD (A-C), cryo-electron tomography of a freeze-etched *Chlamydomonas* axoneme (D,E), and additional features and electron densities visible in the tomographic averages of *Chlamydomonas* axonemes (F-I). (A-C) This sequence of images demonstrates the process of graphically modeling in the IMOD program. The user can display and move between selected slices of the tomographic

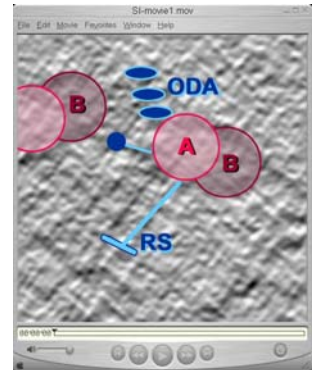
volume with any desired orientation of the slice (A). One then manually outlines and models the visible electron densities (dark) that are representative of protein structures, using different colors to display distinct structures (B). The graphic model can then be displayed, zoomed and rotated for analysis (C); outer (*ODA*) and inner dynein arms (*IDA*, 2-6). **(D,E)** Correlation of our cryo-electron tomography data with previously published rapid-freeze, deep-etch, rotary-replication studies proved to be difficult or at least ambiguous. To reduce the “gap” between these techniques we used an approach that is a hybrid of the two methods, seeking to better understand how these data could be correlated. We freeze-etched quick-frozen axonemes of *Chlamydomonas* by sublimating a small amount of vitreous ice from the sample in the microscope. Instead of metal shadowing the surface of the specimen and using the replica for imaging, however, we used cryo-electron tomography to reconstruct the 3D volume of the remaining ice-layer and the exposed protein structures. The tomographic slices show a freeze-etched *Chlamydomonas* axoneme (*pf9*-mutant) in longitudinal orientation. In both the overview (D) and the close-up view (E) one can see the axonemal structures with unusually high contrast for a raw cryo-tomogram; see e.g. the diagonal OOD-linkers (*white arrowheads*). This suggests that freeze-etching (and metal-shadowing) increase image contrast and can therefore provide useful information about axoneme structure. However, some regions of the freeze-etched axoneme showed flattening; we found that these regions can display heterogeneity of structure preservation and distortions. *Black arrowhead*, OOD-linker; *CPC*, central MT singlets with associated complex; inner (*IDA*, 2-6) and outer (*ODA*) dynein arms; *RS*, radial spokes. **(F-H)** Graphical models of 96 nm repeats showing IDA tails (*T*, *red*) and additional densities not described in previous images (*green* in G,H). Proximal is right in (F), left in (G), and (H) is viewed from distal to proximal; *IA4*, inner dynein arm #4. **(I)** Image similar to (Fig. 5C), but viewed from the opposite side, i.e. from proximal to distal; in this orientation the 1- β DHC of the I1 dynein is not obscured by the IC/LC-complex of the I1 complex and the DRC. Note that all dynein motor domains lie at the same distance from the adjacent B_t-tubule (dashed segment), independent of their position in the inner or outer dynein row. This suggests that they could all interact with the B_t-tubule and contribute to the force production. *A_t*, A-tubule; 6, inner dynein arm #6. Scale: 100nm (D), 50nm (E).

References:

- S1. B. H. Gibbons, *Methods Cell Biol.* **25**, 253 (1982).
- S2. M. E. Porter, J. Power, S. K. Dutcher, *J. Cell Biol.* **118**, 1163 (1992).
- S3. S. H. Myster, J. A. Knott, E. O'Toole, M. E. Porter, *Mol. Biol. Cell* **8**, 607 (1997).
- S4. J. Dubochet *et al.*, *Q. Rev. Biophys.* **21**, 129 (1988).
- S5. D. N. Mastronarde, *J. Struct. Biol.* **152**, 36 (2005).
- S6. J. R. Kremer, D. N. Mastronarde, J. R. McIntosh, *J. Struct. Biol.* **116**, 71 (1996).
- S7. J. Walz *et al.*, *J. Struct. Biol.* **120**, 387 (1997).
- S8. F. Forster, O. Medalia, N. Zauberman, W. Baumeister, D. Fass, *Proc. Natl. Acad. Sci. U.S.A.* **102**, 4729 (2005).

Video Legends Movies S1 to S6:

Movie S1) Movie illustrating the process of particle averaging. Each movie frame displays a tomographic slice through a *Chlamydomonas* doublet microtubule (MT); from the start to the end of the movie the number of repeats included in the averages increases from 1 to 160. With an increasing number of particles, including ones that lay in the structure at different orientations relative to the axis of tilt and thus to the missing wedge, the signal-to-noise ratio increases and both resolution and contrast become more isotropic. The streaks that appear at diverse orientations show the missing wedge artifacts associated with individual images as they add to the average. A/B, A- and B-tubule; ODA, outer dynein arms; RS, radial spokes.



Movie S2) A display of the averaged image data from a sea urchin sperm axoneme, together with a graphic model of the ODA average, generated with IMOD. This display of planes of image data cut at multiple positions and orientations shows how well the graphic models displayed in the paper fit the data. The colors represent: docking complex (pink), intermediate/light chain-complex (green), Outer-Outer-Dynein-linkers (red and yellow), the dynein motor domains and surrounding structures (blue), A-tubule (gray); initially the MT is viewed from proximal to distal. A thickened MT wall between the A- and B-tubule is highlighted in red inside the MT doublet. The dynein stalk domain was not routinely resolved in our data, but a single stalk is visible at the beginning of this movie.



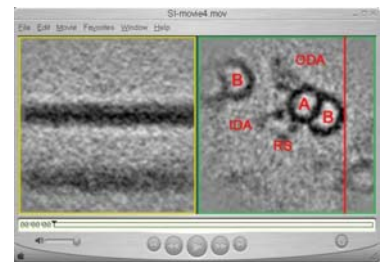
Movie S3) Volume-rendered 96 nm repeat of an outer doublet MT and associated structures, reconstructed from a *Chlamydomonas* wild type axoneme. At various time-points of the movie the I1 complex and nexin link are highlighted.



Movie S4) Same as Movie S3 but from the *pf9*-mutant of *Chlamydomonas*.



Movie S5) Movie of serial tomographic slices cut through the averaged *pf9*-mutant of *Chlamydomonas*: the right image is in cross-section, and the red line indicates the orientation and position of the slice displayed in the left image; the latter is a longitudinal section viewed from the B-tubule of the adjacent doublet.



Movie S6) Movie of the averaged image data together with a graphic model, generated with IMOD, showing a doublet and associated material reconstructed from a *Chlamydomonas* axoneme. The rotating graphical model first summarizes the doublet-associated structures from the *pf9*-mutant, and at the end the I1 complex is indicated in wild type. (For explanation of the colors refer to Figs. 5C,D).

